Ultrafast hot carrier injection in Au/GaN: the role of band bending and the interface band structure

1

Fan Zheng and Lin-wang Wang*

Joint Center for Artificial Photosynthesis and Materials Sciences Division, Lawrence Berkeley National Laboratory, Berkeley, California 94720, USA.

E-mail: lwwang@lbl.gov

2 **Abstract**

3 Plasmon photochemistry can potentially play a significant role in photocatalysis. To
4 realize this potential, it is critical to enhance the plasmon excited hot carrier transfer
5 and collection. However, the lack of atomistic understanding of the carrier transfer
6 across the interface, especially when the carrier is still "hot", makes it challenging
7 to design more efficient system. In this work, we apply the non-adiabatic molecular
8 dynamics simulation to study hot carrier dynamics in the system of Au nanocluster on
9 top of GaN surface. By setting up the initial excited hole in Au, the carrier transfer
10 from Au to GaN is found to be on a sub-pico second time scale. The hot hole first cools
11 to the band edge of Au d-states while it transfers to GaN. After the hole has cooled
12 down to the band edge of GaN, we find some of the charges can return back to Au. By
13 applying different external potentials to mimic the Schottky-barrier band bending, the
14 returning charge can be reduced, demonstrating the importance of the internal electric
15 field. Finally, with the understanding of the carrier transfer's pathway, we suggest

16 that a ZnO layer between GaN and Au can effectively block the “cold” carrier from
17 returning back to Au but still allow the hot carrier to transfer from Au to GaN.

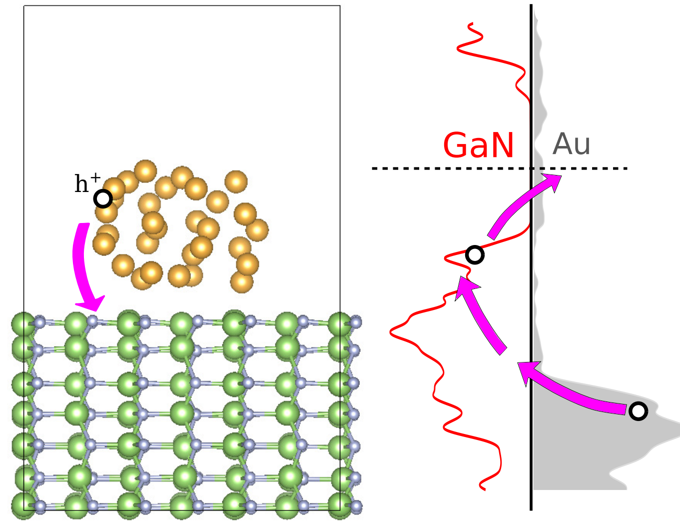
h+
GaN
Au

Photochemistry relies on photo generated carriers to execute electrochemical reactions. Recently, plasmon has been used as a potential photo absorber to generate photo carriers.[1–4] Due to the involvement of many electrons in a plasmon excitation, the plasmon mode in a metal nano-system can have much higher optical oscillator strength than a typical semiconductor, thus it has higher light absorbing efficiency. It has also been shown recently that the collective many-particle plasmon excitation can convert its energy into single-particle excitation inside the metal nano-system within 100 fs .[2,5] One way to harvest such single particle hot carrier is to attach the metal nano-system (e.g., a metallic quantum dot, QD) to a semiconductor substrate. In this case, the hot carrier cooling process is accompanied by carrier injection and carrier transfer into semiconductor substrates. Questions arise for the carrier injection process: (1) what determines the competition between the carrier cooling inside the metal-QD and the carrier injection into the substrate? (2) Can the substrate harvest hot carrier instead of equilibrium ones ("cold" carrier) at the band edge, which can be used to drive the hot carrier nonequilibrium reaction? (3) What is the typical time scale for cooling and carrier injection? (4) How the interface electronic structure and band alignment influence the hot carrier injection? Answering these questions are important. For example, a lot of recent effort has been placed to study the possibility of hot carrier catalysis in various redox reactions such as water splitting and oxidation,[6–11] H_2 decomposition or production,[12–14] and CO_2 reduction.[15–17] Thus, designing an efficient way to harvest hot carriers (not just the "cold" carrier) becomes an important research topic.

The reported efficiencies of the plasmon assisted catalytical reactions are generally low.[18–21] Less than 3% solar-to-chemical efficiency is obtained in CsS-Au-TiO_2 sandwich system,[18] which is far below the solar cell light conversion efficiency. In an Au/TiO_2 system, the efficiency of the light induced carrier transferred is only 0.2%.[21] It is possible that only a small portion of hot carriers has been injected into the carrier collection material during their cooling. The transient pump-probe experiments using absorption spectroscopy or non-linear optics techniques show that the time scale of the charge transfer from a quantum dot or

45 metal cluster to a semiconductor is on the order of sub-pico second.[22–28] However, the exact
46 pictures of such carrier injection and carrier cooling processes are difficult to probe experi-
47 mentally. To understand such process in the atomic scale, theoretical simulation has been
48 used to study this process .[29–33] For example, Atwater et al estimate the surface plasmon
49 decay rate and the initial hot-carrier distribution in metals using Fermi's golden rule.[29,30]
50 Meanwhile, Bernardi et al using perturbation and first-principle method to illustrate plas-
51 mon's decay into hot carriers in noble metals.[34] They also investigate the ultrafast hot carrier
52 dynamics in bulk GaN[35] evaluated by first-principle method based on electron-electron and
53 electron-phonon scattering. Combining with the Boltzmann equation, the carrier mobility
54 and carrier cooling process are revealed in the bulk system. While such methods are excel-
55 lent in studying bulk systems, interfaces of a complex system becomes a challenge due to
56 the high cost of these methods. Thus, it might be difficult to study the carrier injection
57 in a heterogeneous nano-system. Another analytical approach to study carrier injection is
58 to calculate charge transfer rate with formula like the Marcus theory.[36–40] However, these
59 calculations can only reveal charge transfer for localized carriers and for equilibrium cold
60 carriers instead of hot carriers.

61 One alternative approach is to simulate the hot carrier cooling and injection directly using
62 nonadiabatic electronic dynamics. In this approach, the time-dependent Schrödinger's equa-
63 tion is followed to directly simulate the change of carrier wavefunction. It is suitable to study
64 nano-systems with about one hundred atoms, thus it is complementary to the analytical stud-
65 ies based on bulk behaviors.[29,30] Pioneer works based on non-adiabatic molecular dynamics
66 or time-dependent density function theory have studied the carrier motion for interfacial sys-
67 tems, such as Dye-sensitized TiO_2,[41,42] Ag (and Au) on MoS_2,[43] Au nanoparticle/nanorod
68 on TiO_2,[44,45] PbSe nanoparticle on TiO_2,[46] bilayer two-dimension heterostructures,[47] and
69 graphene on TiO_2.[48] They all demonstrate the fast carrier transfer within a few hundreds
70 femtosecond across the interface. However, most of these works illustrate the details of
71 the electron transfer from the band edge of a quantum dot, semiconductor or dye to an-

72 other semiconductor.[41,42,46] Some other works also demonstrate the delocalization across the
73 metal/semiconductor interface from a plasmon-like adiabatic state near the Fermi level.[44,47]
74 However, in most cases, the transferred carriers are band edge carrier, instead of hot carriers.
75 There are not enough studies of the hot carrier cooling in combination of charge transfer. On
76 the other hand, many works[45,49–51] use nonadiabatic molecular dynamics to study hot carrier
77 cooling (e.g. inside a QD), but no injection process. Thus, there is a lack of study to reveal
78 the competition between hot carrier's cooling and hot carrier injection, and different path-
79 ways for hot carrier injections. Furthermore, although Schottky barrier and its related band
80 bending exist in almost all the metal-semiconductor interfaces, a detailed understanding for
81 the role of the Schottky barrier to the carrier transfer is also lacking.

82 In this work, inspired by the recent experimental work of Au nanocluster on GaN for
83 the plasmon hot carrier injection,[16] we use the non-adiabatic molecular dynamics (NAMD)
84 to reveal the details of the hot carrier's cooling and its injection from the Au metal to the
85 GaN substrate. Our NAMD is based on a newly developed algorithm called P-matrix for-
86 malism.[52,53] Unlike previous NAMD methods where multi-trajectory stochastic simulations
87 are used to represent the ensemble of the trajectories to include the detailed balance and
88 decoherence effect,[42–44,46–48] in our P-matrix formalism, a single run can represent a whole en-
89 semble result while including the detailed balance and decoherence effect. In this formalism,
90 the decoherence can be introduced naturally, and detailed balance is also satisfied. The effi-
91 ciency of this new algorithm allows us to study various situations for relatively large systems
92 and relatively long simulation times. By studying the detailed process of the hot carrier's
93 pathway, different sizes of the system, different strength of the applied electric field, and
94 addition of a hole-blocking layer, our simulation reveals the competitions between different
95 relaxation channels, and finds a surprising result of fast carrier injection from Au nanocluster
96 to GaN substrate before the carrier cooling down. After arriving at GaN band edge, some
97 carriers return back to Au nanocluster. Such detailed picture of the hot carrier transfer can
98 help us design more efficient systems to enhance the hot carrier injection efficiency.

99 In our NAMD simulation, we first perform a density functional theory (DFT) ground state
100 Born-Oppenhaimer molecular dynamics (BOMD) simulation. Its nuclear trajectory and the
101 time-dependent Hamiltonian $\mathbf{H}(t)$ is then used to carry out the time evolution of the wave
102 function following the time-dependent Schrödinger's equation: $i\partial\psi(t)/\partial t = \mathbf{H}(t)\psi(t)$. Differ-
103 ent from other NAMD methods, the time-dependent Schrodinger's equation is reformulated
104 following the P-matrix equation in a density matrix formalism.[52] In this way, it is possible to
105 take into account the detailed balance and decoherence effect at the same time. The detailed
106 balance is important in order to describe the cooling process, while the decoherence (dephas-
107 ing) also influences the cooling rate. In this approach, we have ignored the back reaction
108 from the electron movement to the nuclear movement. This approximation is also called
109 classical path approximation (CPA) which are widely used in other NAMD methods.[42,43,47]
110 Such CPA is appropriate for relatively large systems when hot carriers not highly localized,
111 thus the back reaction from the electron movement to the nuclear movement is negligible,
112 and the main interest of study is at the electron dynamics, not the nuclear dynamics.

113 Fig. 1a shows the system we have constructed. The non-polar surfaces $[11\bar{2}0]$ of GaN
114 attaching the Au nanocluster is used to avoid surface reconstruction.[54] Since the structure
115 of the Au nanocluster on GaN in the experiment is not clear, we obtain the Au nanocluster
116 with 30 Au atoms via a simulated annealing using *ab initio* MD (see Methods for details
117 of DFT calculation) where the temperature is initially increased up to 1100 K and then
118 cooled down slowly. A relaxation of the whole system is then performed. Here, the 30-
119 Au-atom nanocluster may not be big enough to generate plasmon oscillation. However, as
120 we will show later about the results of different sizes of Au nanocluster, the hot carrier's
121 pathways of a bigger nanoclusters should be similar to the one we present in this work. The
122 calculated density of states is shown in Fig. 1b, where the Fermi level of Au is within the
123 band gap of GaN. Semi-local functional such as GGA used here is known to predict wrong
124 position of Au *d*-state to its Fermi energy and the band alignment between the Au and
125 GaN states. In addition, the possible electron-hole interaction such as excitonic effect may

126 also be missing in current NAMD implementation. High level calculation such as *GW* and
127 hybrid functional may predict more accurate energy levels. However, these methods become
128 too expensive to run thousands of MD steps. Here, the pseudopotential of Au has been
129 modified so that the position of *d*-orbitals in terms of the Fermi level are consistent to the
130 experiment[55] (see Supporting Information (SI)). Although DFT tends to underestimate work
131 function and ionization energy for Au nanocluster and GaN surface, respectively, we find
132 that their energy level difference for Au and GaN calculated by DFT is quite consistent with
133 the experiments.[56–59] Therefore, the work function and ionization energy are not corrected
134 here (see SI). Our previous work has demonstrated that the hot carrier can be obtained in
135 *d*-states within 50 fs upon the excitation of the plasmon in Ag_{55} nanocluster.[5] In this work,
136 we set up initial hot holes at various *d*-states of Au nanocluster and perform NAMD to
137 investigate their dynamics.

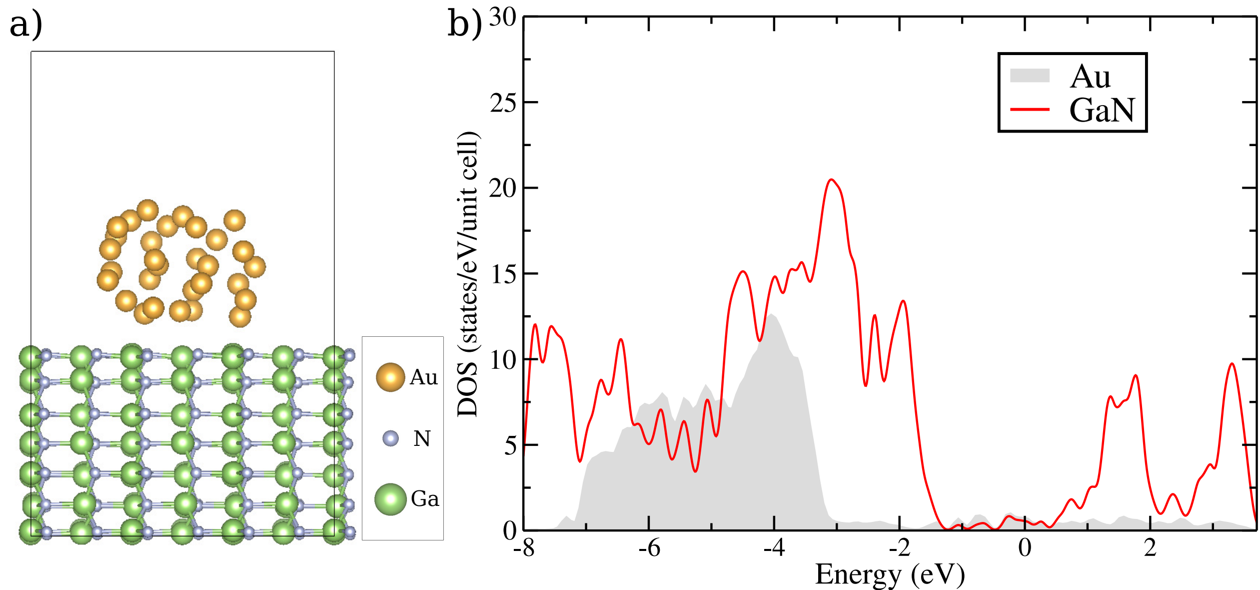

Figure 1: a) Structure of Au/GaN system under simulation (relaxed at 0K). It has 30 Au atoms and 252 GaN atoms. b) Density of states of the 0K structure projected to GaN and Au, respectively. Fermi energy is set at energy 0 eV.

138 In our NAMD simulation, the system is firstly simulated with a Born-Oppenheimer elec-
139 tronic ground state molecular dynamics (BOMD) at room temperature (300K). Then the
140 evaluation of the carrier wavefunction is done as a post-process. The hot-carrier wavefunction

141 $\psi_l(t)$ is evolved following the Schrödinger's equation, and it is expanded with the adiabatic
142 basis $\phi_i(t)$ as $\psi_l(t) = \sum_i C_i^l \phi_i(t)$. Using the density matrix formalism, the density matrix of
143 the system is $D_{ij}(t) = \sum_l w_l C_i^{l*}(t) C_j^l(t)$, under the basis of $\phi_i(t)$, where w_l is the weight of ψ_l.
144 Due to this w_l, a $D_{ij}(t)$ can represent an ensemble of wavefunction trajectories. Following
145 the time-dependent Schrödinger's equation, the equation of motion for the density matrix
146 can be written down as:[52]

$$\frac{\partial}{\partial t} D_{ij}(t) = -i \left[V(t), D(t) \right]_{ij} - (1 - \delta_{ij}) \frac{D_{ij}(t)}{\tau_{ij}(t)} \tag{1}$$

147 and $V_{ij}(t) = \delta_{ij}\epsilon_i(t) - i \langle \phi_i(t) | \partial \phi_j(t) / \partial t \rangle$ contains the information of the change of adiabatic
148 state $\phi_i(t)$, which implicitly includes the effect of the electron-phonon coupling. The second
149 term is used to introduce the decoherence where $\tau_{ij}(t)$ represents the decoherence time
150 between state i and j. To introduce the detailed balance, a P-matrix formalism is used
151 where the density matrix $\mathbf{D}$ is splitted into $\mathbf{D} = \mathbf{P} + \mathbf{P}^{\mathrm{T}}$ (see details in Method). The
152 evolution of $\mathbf{P}$ matrix is illustrated in **Methods** as equation 5 and equation 6. To integrate
153 the equation of motion for these two equations, a small time step dt is used from T_n to T_{n+1},
154 where T_n is the n-th MD step. Thus, $H_{ij}(t)$ matrix is diagonalized at every dt step between
155 T_n and T_{n+1} to get its adiabatic states $\phi_i(t)$ under the basis of $\phi_i(T_n)$, and $\phi_i(t)$ is used to
156 evaluate $V_{ij}(t)$. In our system, N is more than 300. In practice, it is still a challenge to
157 integrate $\mathbf{P}(t)$ from T_n to T_{n+1} at every dt step following equation 5 and 6 (see Methods).
158 This is because a small dt is needed due to the possible sharp peaks in evaluating $V_{ij}(t)$
159 caused by the derivative $\partial \phi_j(t) / \partial t$. This happens when two $\phi_j(t)$ states cross each other,
160 thus their identities exchanged. Although MD step can be set as 1 or 2 fs, a very small dt
161 (< 0.0005 fs) must be used for carrier's dynamics, which can result in several thousand steps
162 between T_n and T_{n+1}. Since each t step requires a $N \times N$ matrix diagonalization of $H_{ij}(t)$ to
163 get $\phi_i(t)$ to evaluate $V_{ij}(t)$, this can be quite expensive. For a complex system with several

164 hundreds adiabatic states like the interfacial system we are studying, the NAMD simulation
165 can take days even to accomplish a few MD steps.

166 To solve this problem, in the current study, we have modified the implementation of
167 NAMD. Instead of diagonalizing the Hamiltonian every dt step from T_n to T_{n+1}, we split
168 $dT = T_{n+1} - T_n$ into M time-intervals with equal length $\delta t = dT/M$ (M is around 100 and δt
169 is in the order of 0.01 fs). The start of each time-interval is labeled as t_m (thus $t_m = T_n + m\delta t$)
170 with $m = 0, 1, ..., M$. In the modified NAMD, during one δt time-interval from t_m to t_{m+1},
171 instead of using $V_{ij}(t)$, the $\mathbf{P}$ matrix will be evolved using a fixed basis set $\phi_i(t_m)$ which
172 is the adiabatic eigen state obtained at time t_m.The corresponding equation is equation 2.
173 From t_m to t_{m+1}, there is no need for matrix diagonalization, and $\mathbf{H}(t)$ is obtained from
174 interpolation under the basis $\phi_i(t_m)$. The diagonalization of the Hamiltonian is only needed
175 at the start of each time-interval (t_m) to obtain the basis $\phi_i(t_m)$. In this way, the number
176 of diagonalization operations can be reduced from several thousands to only 100 within one
177 MD step dT. More specifically, we have:

$$\frac{\partial}{\partial t} P_{ij,m}(t) = -i \left[H_m(t), P_m(t) \right]_{ij} . \tag{2}$$

178 for $t \in [t_m, t_{m+1}]$. Here, $\mathbf{H}_m(t)$, $\mathbf{P}_m(t)$ mean the matrix under the basis of $\phi_i(t_m)$. Thus,
179 if we have solved $\phi_i(t_m) = \sum_j S_{ij}(T_n, t_m)\phi_j(T_n)$ ($\mathbf{S}_m(T_n, t_m)$ is the eigen-vector of the diag-
180 onalization performed at time t_m), $\mathbf{H}_m(t) = \mathbf{S}(T_n, t_m)\mathbf{H}_{T_n}(t)\mathbf{S}^\star(T_n, t_m)$, and $\mathbf{H}_{T_n}(t)$ is the
181 interpolated Hamiltonian under $\phi_i(T_n)$ basis. To evolve equation 2 from t_m to t_{m+1}, not only
182 one does not to diagonalize the Hamiltonian, there is also no sharp peaks to $\mathbf{H}_m(t)$. It makes
183 the time evolution relatively easy. At time t_{m+1}, one diagonalizes the $\mathbf{H}_{T_n}(t_{m+1})$ to obtain
184 $\phi_i(t_{m+1})$, then converts $\mathbf{P}_m(t_{m+1})$ to $\mathbf{P'}_{m+1}(t_{m+1}) = \mathbf{S}(t_m, t_{m+1})\mathbf{P}_m(t_{m+1})\mathbf{S}^\star(t_m, t_{m+1})$. Here,
185 $S_{ij}(t_m, t_{m+1}) = \langle \phi_i(t_m) | \phi_j(t_{m+1}) \rangle$. After this step, the decoherence and detailed balance can
186 be added as:

$$P_{ii,m+1}(t_{m+1}) = P'_{ii,m+1}(t_{m+1}) + \sum_j \mathrm{Re}\left[\langle\phi_j(t_m)|\phi_i(t_{m+1})\rangle\, P'_{ij,m+1}(t_{m+1})\right] f_{ij}\left(e^{-|\Delta\epsilon_{ij}|\beta} - 1\right) \tag{3}$$
$$- \sum_j \mathrm{Re}\left[\langle\phi_i(t_m)|\phi_j(t_{m+1})\rangle\, P'_{ji,m+1}(t_{m+1})\right](1 - f_{ij})\left(e^{-|\Delta\epsilon_{ij}|\beta} - 1\right)$$

187 for diagonal element of P_{ii}, and

$$\begin{aligned} P_{ij,m+1}(t_{m+1}) &= P'_{ij,m+1}(t_{m+1}) \\ &- \langle\phi_i(t_m)|\phi_j(t_{m+1})\rangle\, P'_{ii,m+1}(t_{m+1}) + \langle\phi_i(t_{m+1})|\phi_j(t_m)\rangle\, {P'_{jj,m+1}}^*(t_{m+1}) \\ &- P'_{ij,m+1}(t_{m+1})\frac{t_{m+1} - t_m}{\tau_{ij}} \end{aligned} \tag{4}$$

188 for off-diagonal elements P_{ij} $(i \neq j)$. Such $\mathbf{P}_{m+1}(t_{m+1})$ will be the starting point for the
189 next $[t_{m+1}, t_{m+2}]$ interval calculation using equation 2. Note, in equation 3 and 4, the
190 $\langle\phi_i(t_m)|\phi_j(t_{m+1})\rangle$ term is used to approximate $V_{ij} \cdot (t_{m+1} - t_m)$ term in equation 1 (and
191 equation 5 and 6). To evaluate equation 2 from t_m to t_{m+1}, high order expansion of $e^{i\mathbf{H}dt}$ can
192 be used. We find higher orders give negligible improvement over the first-order formalism.
193 The equation 2-4 are approximations of equation 5 and 6. In reality, our test shows that
194 the results using equation 2-4 are almost indistinguishable from the results by equation 5
195 and 6, as shown by an example in SI Fig.6 with the averaged hole energy as a function of
196 time computed by these two methods. However, the new equations can be hundreds of times
197 faster if large basis set N is used. From the density matrix $\mathbf{D}$, the charge density of system
198 at time t can be computed as $\rho(\mathbf{r},t) = \sum_{ij} D_{ij}(t)\phi_i^*(\mathbf{r},t)\phi_j(\mathbf{r},t)$. All the NAMD simulations
199 shown below are tested to converge over dt used in equation 2 (dt is set to be 0.0005 fs) and
200 the number of diagonalizations (value of M) between two MD steps is 100. Although *ab*
201 *initio* MD takes days, the post-processing NAMD only requires a few hours.

202 We choose one of the adiabatic eigen states characterized by Au d-states as the initial

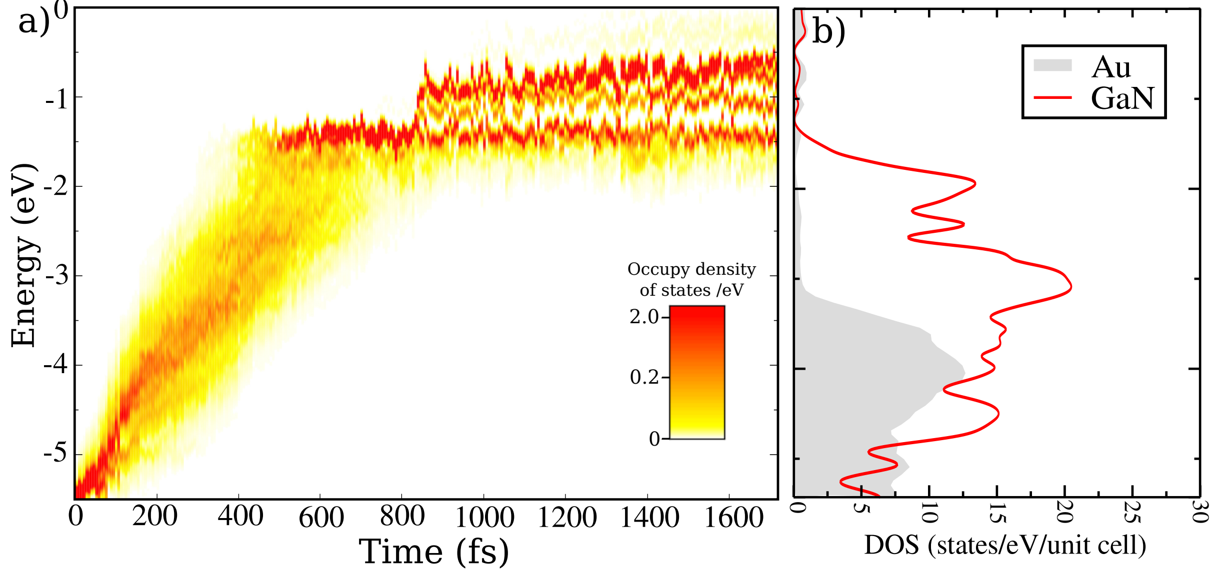

Figure 2: a) Eigen energy of the adiabatic states and their occupation. The color indicates the occupy density of states ($D_{\text{occ}}(E,t) = \sum_i D_{ii}(t)\delta(E-\epsilon_i(t))$ for the excited hole. b) Density of states of the structure at time=0 (same to Fig. 1b). The Fermi energy is set at energy zero.

203 position of the hot hole. For all the NAMD simulations, the initial state is chosen so that
204 more than 85% charges are on Au (see SI Fig.1 for one example). Fig. 2a shows evolution of
205 the energy and the occupation density (defined as $D_{\text{occ}}(E,t) = \sum_i D_{ii}(t)\delta(E-\epsilon_i(t))$ changing
206 with time starting from the initial state. Combining the Fig. 2a with the density of states
207 in Fig. 1b, the whole process can be splitted into three periods: period 1 (from initial hole
208 to around -3.2 eV) possesses the highest hole cooling rate. This is due to the high density
209 of states from both GaN p- and Au d-states. The density of states reduces during period
210 2 (from -3.2 eV to -1.5 eV) because of the low density of states of Au contributed by only
211 its s-orbital in this energy range. However, once the hole cools to the edge of GaN valence
212 bands around 500 fs, the sudden reduction of density of states with only Au s-states slows
213 down the carrier cooling significantly in period 3 (from -1.5 eV to Fermi energy at 0 eV).
214 Particularly, the relatively sparcity of the Au eigen states within the GaN band gap may
215 prevent the carrier from cooling to the Fermi energy within our simulation time due to the

216 phonon bottleneck effect. Since a single-phonon energy is not high enough to satisfy the
217 energy conservation between different electronic states, the carrier has to wait for a long
218 time for a multi-phonon scattering process to jump to lower energy states. We have tested
219 the simulation up to 4 ps, the occupation of the carrier near the Fermi level is still not
220 significant at the end of the simulation. In the above simulation, the initial energy of the
221 hot hole relative to Fermi energy is relatively low compared to the typical laser energy used
222 to excite the plasmon. However, we have also calculated several cases with different initial
223 energies of the hole (all starting from Au *d*-state), they all show similar cooling rate and
224 pathways (SI Fig. 3).

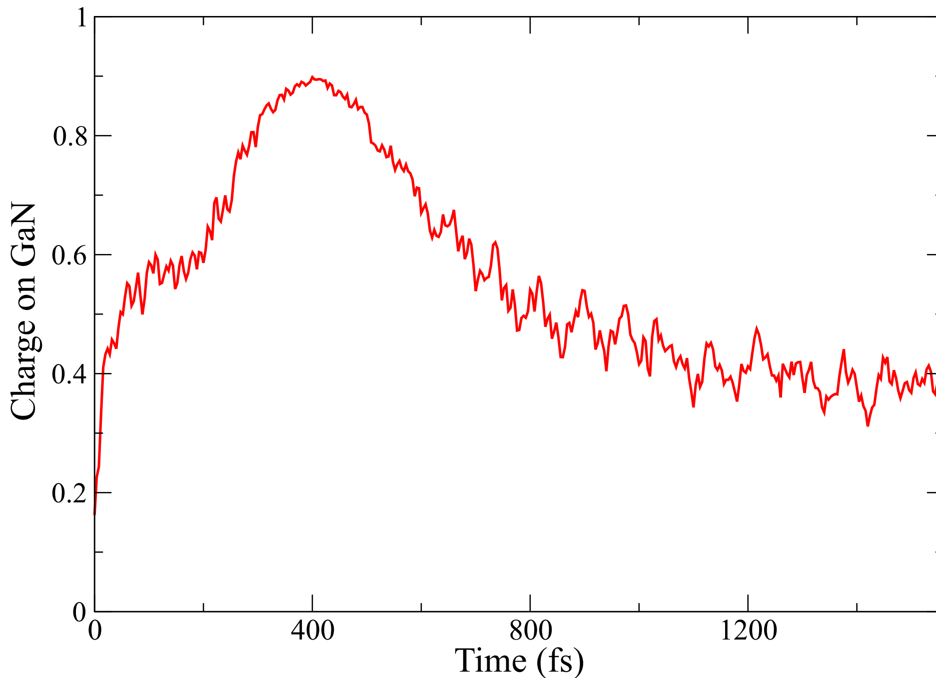

Figure 3: Charge on GaN along with time. The red line is averaged over 20 trajectories. When the charge is counted, charges below the middle line of bottom layer of Au and top layer of GaN are counted as the charge of GaN; otherwise as the charge of Au.

225 In addition to the above energy analysis for the hole's motion, it is possible to analyze
226 its spatial transfer pathways across the interface. In a way, this is already partially shown
227 in Fig. 2, since the density of states (Fig. 2b) illustrates the dominant character of the
228 eigen states within an energy range as GaN, Au or their mix. Fig. 3 shows the charge

229 distributed on GaN as a function of time in a more direct way. Here, we have simulated
230 20 different initial configurations. The curve is the averaged charge distribution over these
231 20 simulations. Note, each P-matrix simulation already includes an ensemble of trajectories
232 starting with the same initial wave function and with the same nuclear trajectory. At the
233 starting point, the majority of the hole-charges are on Au as aforementioned. However, these
234 charges quickly expand to GaN to 50% GaN-occupation within 50 fs. Such fast process is
235 also consistent to previous theoretical investigations.[43,44] From 50 fs to around 200 fs, the
236 occupation of charge on GaN is a rough plateau around 55%. Together with Fig. 2, we find
237 that this period corresponds to the carrier cooling within the Au d-state until it reaches the
238 bottom of d-state (period 1). The 55% occupation may be due to similar density of states
239 between GaN and Au in this energy region (Fig. 2b). Using a larger Au nanocluster will
240 shorten this period. This can be observed in the simulation of a 60-Au nanocluster shown
241 in SI Fig. 5, where the net increase of the density of states caused by larger Au cluster
242 reduces the "plateau" time but also decreases the distribution of charge in GaN during this
243 plateau. After 200 fs in Fig. 3, the hot hole begins to transfer to GaN, and nearly 90%
244 of the hole is inside GaN at around 400 fs. Referring back to Fig. 2a and 2b, one can
245 see that starting from around 300fs, at the hot carrier's energy region, the Au only has
246 its s-state density of states, and the majority of the density of states comes from GaN. At
247 around 400 fs, the carrier reaches the top of the valence state in GaN, and the maximum
248 occupation in GaN is also reached. After 400 fs, the occupation inside GaN begins to reduce,
249 indicating a back-flow to Au for it to reach the Fermi energy in Au. Overall, our simulation
250 demonstrates that the *majority* of the hot hole tends to cross the interface quickly instead
251 of waiting inside Au until it has cooled down to the edge of d-state and all the way to the
252 Fermi energy. The carrier immediately spreads out to GaN before it is cooled down to the
253 bottom of Au-d states. Although Au nanocluster is only weakly binded to GaN, the vdW
254 nature of the interaction does not prevent the hole-charge from jumping from Au to GaN.
255 One might wonder whether this fast spread of carrier localization is due to the small size of

256 the simulated Au cluster, which might be difficult to contain the carrier wavefunctions (SI
257 Fig. 1a). But the similar behavior is observed when we increase the Au nanocluster size
258 from 30 to 60 atoms. As shown in SI Fig. 5, the Au 60-atom case is much alike the Au
259 30-atom case. Nevertheless, we do see some differences. First, the maximum transfer charge
260 to GaN has reduced slightly from 90% to 85%, and the charge plateau before the carrier
261 reaches the top of Au-d states has also reduced from about 55% to 45%. But note that all
262 these reduction is not inversely proportional to the Au nanocluster size, which has doubled
263 from 30 atoms to 60 atoms. Comparing Fig. 3 with SI Fig. 5, the biggest difference comes
264 from the time to reach the maximum. Roughly, the cooling rate in the Au 60-atom case is
265 twice as fast as the case in Au 30-atom case. This means that small Au 30-atom nanocluster
266 suffers strongly from its phonon-bottleneck effect, and the electron-phonon coupling inside
267 the Au nanocluster dominates the initial cooling process, despite the fact more than half of
268 the carrier wavefunction is outside the Au nanocluster.

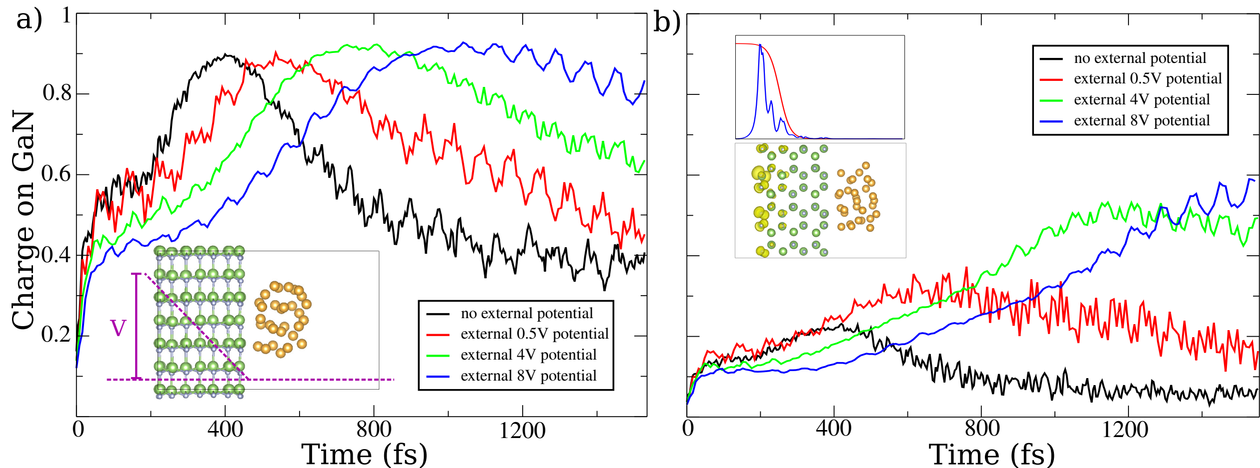

Figure 4: a) Total hole charge in GaN under different external potentials. Inset: the scheme of the applied external potential. b) Charge occupation in the mask region under different external potentials. Inset: (bottom) localized charge density of one adiabatic state under the external potential of 8V, (top) its charge density averaged in x-y plane (blue curve), and the mask function (red curve). To simplify the analysis, charges below the middle line between bottom layer of Au and top layer of GaN are treated belonging to GaN; otherwise they will be counted as charge of Au.

269 After the majority of the hole are transferred to GaN, we observe that some holes return

270 back to Au after they cool down to the valence band edge of GaN. In Fig. 3, the hole
271 distribution on GaN starts to decrease to only around 40% from 400 fs up to 1200 fs. It
272 shows that less than half of the holes stay on GaN, but other holes return back to Au.
273 Such back transfer has been observed in previous experimental and theoretical works.[22,42,44]
274 Particularly, the nonlinear optical technique reveals the returning of the transferred electron
275 is on picosecond time scale,[22] closing to the time of the hole's returning in our calculation.
276 Thus, it is something to be prevented since it reduces the eventual carrier harvesting. It
277 will be quite useful to engineer the interface to reduce this back transfer. Before we discuss
278 different ways to mitigate this back flow, it is worth to discuss first the possible artifacts
279 which contribute to this back flow. In a real system, when the charge is transferred out of
280 Au, it can move into the bulk of GaN far away from Au nanocluster, thus never returns. To
281 show the back flow due to the finite size of the system, we perform a simulation of the same
282 system but putting the initial hole in the GaN above the *d*-state of Au (see SI). We find that
283 the "warm" hole (its energy is above the Au *d*-state) spreads from GaN to Au in very similar
284 fashion as the back transfer case shown in Fig.3 (SI Fig.4). Our calculation demonstrates
285 that the back flow is non-avoidable given the small GaN layer we can afford. We believe due
286 to the limited GaN layers in our simulation, the effect of back flow is probably overestimated.
287 Nevertheless, we should still be able to design heterostructures to enhance the hole transfer
288 to GaN, as the qualitative trend should still be the same. The relative values of the back
289 flow to Au should still be a good indicator.

290 The experiments of the heterostructure Au/p-type GaN illustrated in Ref. 16 and 23
291 demonstrate the hole harvesting from Au to GaN. The Schottky-barrier band bending in
292 this system has been shown to play a central role to assist the hole transfer. The careful
293 design of such heterostructure allows the formation of the internal electric field near the
294 interface resulting from the band bending in the depletion layers. Such electric field can
295 drive the hole away and reduce their back transfer. In order to demonstrate the role of
296 the internal electric field, we perform MD and NAMD simulations under different external

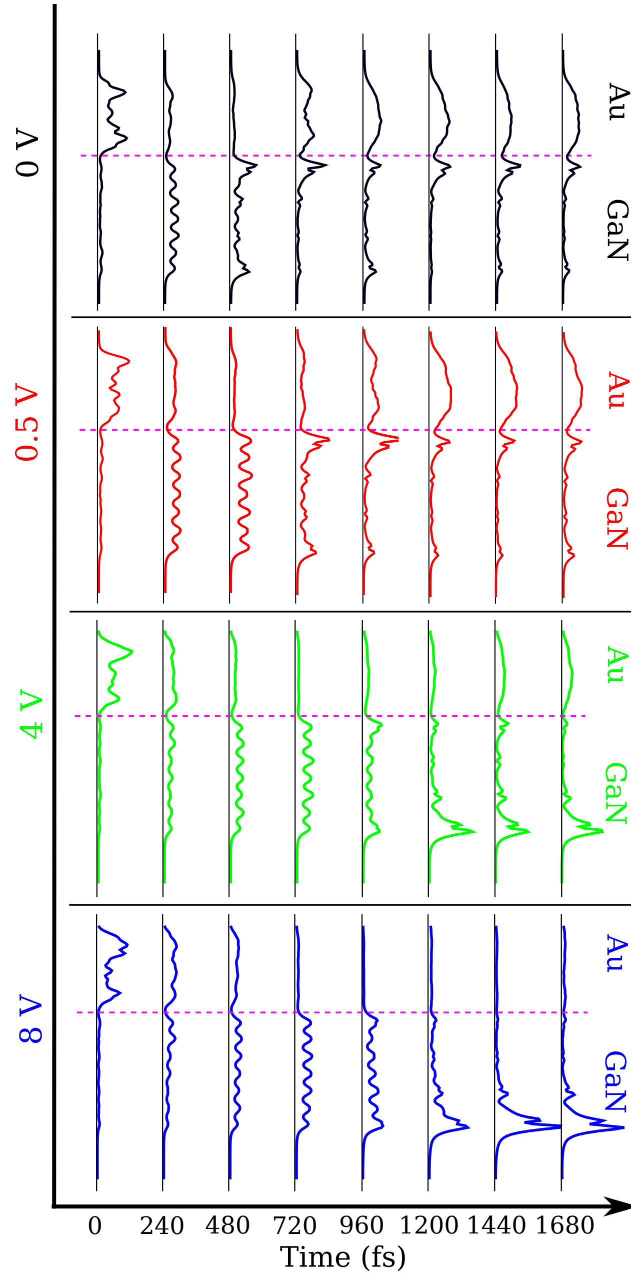

Figure 5: Charge density evolution with time under different external potentials (from top to bottom, 0V, 0.5V, 4V and 8V). Dashed magenta line separate Au and GaN regions. The charge density is averaged in $x-y$ plane of the simulation cell as $\rho(z;t) = \int \rho(x,y,z;t)dxdy$.

297 electric fields. Shown in Fig. 4a inset is the scheme of the external potentials added to
298 mimic the Schottky barrier band bending. External potentials with values of 0.5V, 4V and
299 8V at the vacuum side end of GaN are applied linearly inside GaN, respectively. For all
300 these cases, the states near the Fermi energy are still Au states. Thus, thermadynamically,
301 the hole should still return to Au. Fig. 4a shows the spatial charge occupation on GaN as a
302 function of time under different external potentials. It is interesting to see that by applying
303 higher electric field, more holes tend to stay on GaN for a longer time, less likely to return to
304 Au. Even a relatively low external potential of 0.5V can affect the behaviour of the excited
305 hole noticeably. It is also interesting to see that the time of the charges arriving at GaN also
306 becomes slower when the field strength increases. This is due to a shift of GaN density of
307 state. The lack of density of states at higher electric field reduces the initial charge transfer
308 rate. In order to further understand the charge distribution inside GaN. Fig. 4b illustrates
309 the charge distribution of the localized adiabatic state within a "mask" region at the end
310 of GaN in its vacuum side as shown in the inset. We use a mask function to capture such
311 state. This mask $m(\mathbf{r})$ is then used to calculate $\int \rho(\mathbf{r},t)m(\mathbf{r})d^3\mathbf{r}$, and the result is shown
312 in Fig. 4b. As we have discussed above, our calculation may overestimate the amount of
313 the charge returning to Au and have almost 100% return of the charge to Au if the running
314 of our calculation is infinitely long, since the states at Fermi energy is localized inside Au.
315 It is thus helpful if we can define a measure of charge density inside GaN, and assume the
316 measured charge to disappear into the bulk of GaN in an infinite GaN system. One such
317 measure is the trapped charge within that mask. It is reasonable to assume that once the
318 charge is "trapped" in this mask region, it can be considered as going to the bulk GaN, and
319 never returns. Thus, we can use the highest amplitude of the charge inside the mask region
320 during the simulation time to provide a quantitative measure of the total charge captured by
321 the bulk GaN. The subsequent decay of the charge within the mask region is due to the back
322 flow to higher energy Au state owing to the finite size of the simulated system. Note, this is
323 probably a lower-limit estimation, since before it reaches the maximum, some of the charge

324 might already return to the Au due to the finite GaN size (hence once again, overestimation
325 of the back flow). Besides, the mask function itself only calculates the state near the end of
326 GaN, thus can miss other states of GaN. Nevertheless, we can use these numbers to provide
327 an estimate. Under the external potentials of 0, 0.5, 4, and 8V, we get the maximum charge
328 of 22%, 35%, 50% and 60%, respectively.

329 To further understand the details of the charge distribution in real space, Fig. 5 illustrates
330 the charge density chosen from one initial state run averaged over x-y plane under different
331 external potentials (from top to bottom: 0V, 0.5V, 4V and 8V) as a function of time.
332 All the cases show a sub-picosecond fast charge transfer from Au to GaN. For 0 V, the
333 charges on GaN never stay significantly in the mask region. For 0.5 V case, there is a
334 slight distribution in this region, but most of the charge escapes to Au eventually. When
335 the electric field increases further, the mask regions start to be populated clearly after the
336 charges are transferred to GaN, indicating the efficiency of the band bending to assist the
337 hole transfer in Au/GaN heterostructure.

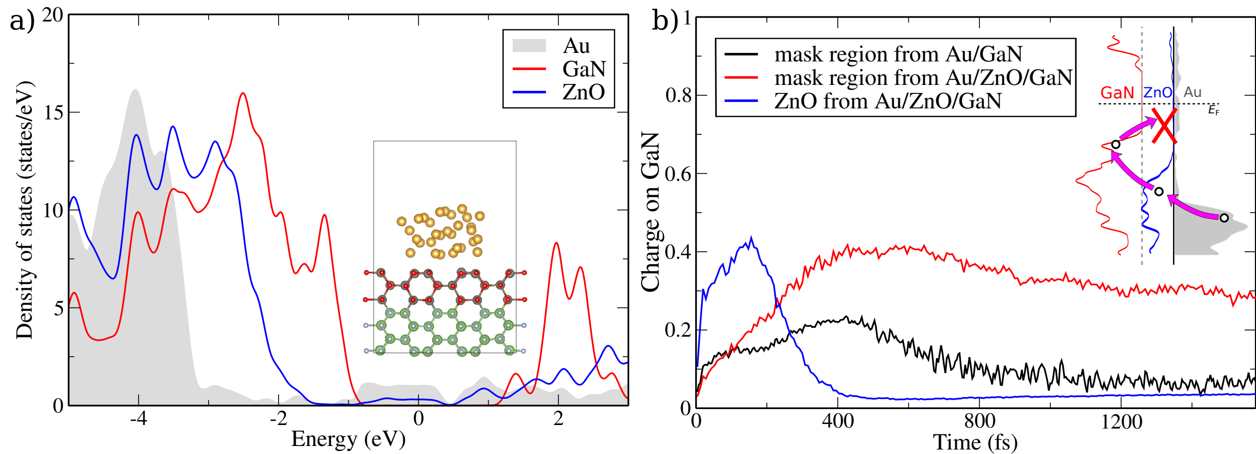

Figure 6: a) The projected density of states of Au, ZnO and GaN. Inset: relaxed structure of Au/ZnO/GaN heterostructure at 0K (Red: oxygen atom, Dark grey: zinc atom). b) The charge distribution of GaN and ZnO compared to the pure Au/GaN system. The mask region is the same to the pure Au/GaN case (Fig. 4b). Inset: illustration of the role of ZnO in preventing the hole from returning back to Au after it reaches the band edge of GaN. But the initial hot hole transfer from Au to GaN is not affected by ZnO.

338 In addition to the Schottky barrier and its induced internal electric field, following our

339 understanding of the charge back flow, we propose to use a hole-block layer to prevent the
340 back flow. Such inserted layer separates GaN and Au wavefunction spatially to reduce their
341 coupling, hence to prevent the back flow of the equilibrized hole carrier. On the other hand,
342 the inserted layer should have a potential barrier low enough so that it will not block the
343 initial hot carrier transfer from Au to GaN. We find ZnO is a good choice. Similar to
344 GaN, ZnO possesses wide band gap. Its valence band maximum is around 0.8 eV lower
345 than that of GaN, roughly at the same level of *d*-states edge of Au.[57] Interestingly, ZnO
346 has quite similar structure (Wurtzite crystal shape) and lattice constants to GaN, which
347 brings a great advantage for high quality synthesis as well as theoretical simulation. In our
348 calculation, we replace top three layers of GaN by ZnO (Fig. 6a inset), relax the whole
349 structure, and compute the projection of the density of states. Fig. 6a shows the position
350 of the ZnO states, which is consistent to the experiments.[56,57,60,61] By performing MD and
351 post-processing NAMD simulations, the time-dependent spatial charge distribution on GaN
352 is obtained, and shown in Fig. 6b. Similar to the case of Au/GaN, the hot hole transfers
353 to GaN by passing through ZnO. This initial charge transfer is not significantly reduced
354 by the existence of ZnO. After the charge reaches the band edge of GaN and becomes an
355 equilibrium "cold" carrier, the potential created by ZnO effectively reduces the coupling
356 between GaN and Au, and diminishes the back flow to Au. Using the same approach as
357 for the external potential case, we obtain the maximum amount of charge transfer in the
358 mask region. We get a value of more than 40%, which is much higher than the 22% of the
359 pure Au/GaN structure. The effect of the three layer of ZnO is equivalent to an applied
360 external potential between 0.5 and 4V. Furthermore, when the amount of charges inside the
361 mask region reaches the maximum, its subsequent reduction also becomes slower compared
362 to pure Au/GaN case even with an external potential. It further shows the effectiveness of
363 ZnO layer lowering the back flow from GaN to Au.

364 In summary, we have performed a detailed hot hole dynamics with quantum mechanics
365 non-adiabatic molecular dynamics simulation for the heterostructure Au/GaN. By setting

366 up the hole initially at Au d-state, the *ab initio* MD and the post-processing NAMD reveal
367 that the time-scale for the hole transfer is less than 200 fs. The excited hole first cools to
368 the band edge of Au d-state, while at the mean time spread out into GaN. The majority of
369 the charge then quickly cool down further to the edge of GaN. We also observe that some
370 of the charge can return back to Au after it reaches the band edge of GaN. To understand
371 the role of band bending in Schottky barrier, different external potentials are applied. The
372 NAMD simulation shows that the internal electric field can indeed enhance the hole transfer
373 from Au to GaN. Using a special technique of GaN edge trapping state, we estimate the
374 lower limit of total charge transfer amplitude when the external potential is 0, 0.5, 4 and 8V,
375 as 22%, 35%, 50% and 60%, respectively. We also propose a ZnO insertion layer between
376 GaN and Au to prevent the back flow of the "cold" hole, while keep the initial hot carrier
377 flowing from Au to GaN. We find more than 40% electron transfer to GaN when ZnO layer
378 is used, this is to compare with the 22% electron transfer without the ZnO hole-block layer.
379 Finally, we also find that increasing the Au nanocluster from 30-atom to 60-atom will speed
380 up the hot carrier cooling rate significantly, but only slightly reduce the hot carrier transfer
381 amplitude from Au to GaN. This indicates that the cooling is predominatly caused by the
382 electron-phonon coupling within Au, and the phonon bottleneck plays an important role.
383 Our calculation demonstrates that the newly developed P-matrix method can be used to
384 study carrier dynamics for systems with hundreds of atoms, and to simulate the dynamics
385 for multiple picoseconds.

386 Acknowledgement

387 This material is based on the work performed by the Joint Center for Artificial Photosyn-
388 thesis, a DOE Energy Innovation Hub, supported through the Office of Science of the U.S.
389 Department of Energy under Award number DE-SC0004993. We use the resource of National
390 Energy Research Scientific Computing center (NERSC) located in Lawrence Berkeley Na-

tional Laboratory and the computational resource of the Oak Ridge Leadership Computing Facility at the Oak Ridge National Laboratory under the Innovative and Novel Computational Impact on Theory and Experiment project.

Methods

P-matrix Method. To introduce the detailed balance, a P-matrix formalism is used where the density matrix $\mathbf{D}$ is splitted into $\mathbf{D} = \mathbf{P} + \mathbf{P}^{\mathrm{T}}$ with P_{ij} describing electronic state population transition from state i to j (note $P_{ij} \neq P_{ji}^{*}$). More explicitly, the diagonal elements of the density matrix ($D_{ii} = 2P_{ii}$) evolves as:[52]

$$\begin{aligned}\frac{\partial}{\partial t}P_{ii} = &-\mathrm{Re}\left(i\left[V,P\right]_{ii}\right)\\ &+\sum_{j}\mathrm{Re}\left(iP_{ij}V_{ji}\right)f_{ij}\left(e^{-|\Delta\epsilon_{ij}|\beta}-1\right)\\ &-\sum_{j}\mathrm{Re}\left(iP_{ji}V_{ij}\right)\left(1-f_{ij}\right)\left(e^{-|\Delta\epsilon_{ij}|\beta}-1\right),\end{aligned} \tag{5}$$

while the off-diagonal element of P evolves as:

$$\frac{\partial}{\partial t}P_{ij} = -i\left[V,P\right]_{ij} - iV_{ij}\left(P_{ii}+P_{jj}^{*}\right) - \frac{P_{ij}}{\tau_{ij}} \tag{6}$$

$\Delta\epsilon_{ij} = \epsilon_i - \epsilon_j$, and f_{ij} =1 (0) for $\Delta\epsilon_{ij} > 0$ and f_{ij} =0 (1) for $\Delta\epsilon_{ij} < 0$ for an electron (hole) dynamics. The last two terms in equation 3 introduce the detailed balance, while the last term in equation 4 introduces the decoherence. For details of the derivation, we refer to our previous publications.[52,53] Combining with CPA, a ground state BOMD simulation is first executed. During such simulation, it yields the adiabatic eigen state and eigen energy pairs at MD step T_n as $\{\phi_i(T_n), \epsilon_i(T_n)\}$. The overlapping matrix $S_{ij}(T_n, T_{n+1}) = \langle\phi_i(T_n)|\phi_j(T_{n+1})\rangle$ is recorded. Here the time step dT of BOMD simulation ($dT = T_{n+1} - T_n$) is around 1 or 2 fs. With the overlapping matrix, using the eigen state $\{\phi_i(T_n)\}$ as the basis set, the Kohn-Sham Hamil-

408 tonian at time T_n is: $H_{ij}(T_n) = \epsilon_i(T_n)\delta_{ij}$, while the Hamiltonian at next MD time step T_{n+1}
409 with the *same* basis $\{\phi_i(T_n)\}$ becomes: $H_{ij}(T_{n+1}) = \sum_k S_{ij}(T_n, T_{n+1})\epsilon_k(T_{n+1})S_{ij}{}^*(T_n, T_{n+1})$.
410 Here we assume $S_{ij}(T_n, T_{n+1})$ is a unitary matrix. In practice, a Gram-Schmidth approxi-
411 mation is used to enforce its unitarity. Knowing $H_{ij}(T_n)$ and $H_{ij}(T_{n+1})$ allows us to linearly
412 interpolate the Hamiltonian $H_{ij}(t)$ at any time t within the interval $[T_n, T_{n+1}]$. This effec-
413 tively reduces the original plane wave Hamiltonian to a small $N \times N$ Hamiltonian, where N
414 is the number of $\phi_i(T_n)$ kept in the basis set.[53]

415 **DFT methods.** We perform the plane-wave pseudopotential DFT calculation imple-
416 mented in PWmat package[62,63] with the generalized gradient approximation (GGA) exchange
417 correlation functional.[64] The atomic structure is relaxed prior to molecular dynamics (MD)
418 simulations, and SG15 pseudopotentials[65] are used with 50 Ryd plane wave kinetic energy
419 cutoff. For MD calculation, time step of 2fs is used for all the simulations. The structural
420 optimization reduce forces on all the atoms to be below 0.02 eV/Å.

421 Supporting Information

422 Initial state of hot hole; Energy of the trajectories with different τ; Different positions
423 of the initial states; initial hole starting from GaN; 60-Au-atom system for NAMD; and
424 comparison of original P-matrix method and the improved method used in this work.

425 References

426 (1) Mukherjee, S.; Libisch, F.; Large, N.; Neumann, O.; Brown, L. V.; Cheng, J.; Las-
427 siter, J. B.; Carter, E. A.; Nordlander, P.; Halas, N. J. Hot Electrons Do the Impossible:
428 Plasmon-Induced Dissociation of H2 on Au. *Nano Letters* **2013**, *13*, 240–247.

429 (2) Moskovits, M. The Case for Plasmon-Derived Hot Carrier Devices. *Nature Nanotech-*
430 *nology* **2015**, *10*, 6–8.

431 (3) Clavero, C. Plasmon-Induced Hot-Electron Generation at Nanoparticle/Metal-Oxide

432 Interfaces for Photovoltaic and Photocatalytic Devices. *Nature Photonics* **2014**, *8*, 95–
433 103.

434 (4) Christopher, P.; Moskovits, M. Hot Charge Carrier Transmission from Plasmonic
435 Nanostructures. *Annual Review of Physical Chemistry* **2017**, *68*, 379–398.

436 (5) Ma, J.; Wang, Z.; Wang, L.-W. Interplay between Plasmon and Single-Particle Excita-
437 tions in a Metal Nanocluster. *Nature Communications* **2015**, *6*, 10107.

438 (6) Robatjazi, H.; Bahauddin, S. M.; Doiron, C.; Thomann, I. Direct Plasmon-Driven
439 Photoelectrocatalysis. *Nano Letters* **2015**, *15*, 6155–6161.

440 (7) Zhong, Y.; Ueno, K.; Mori, Y.; Shi, X.; Oshikiri, T.; Murakoshi, K.; Inoue, H.; Mi-
441 sawa, H. Plasmon-Assisted Water Splitting Using Two Sides of the Same SrTiO3
442 Single-Crystal Substrate: Conversion of Visible Light to Chemical Energy. *Angewandte*
443 *Chemie International Edition* **2014**, *53*, 10350–10354.

444 (8) Mubeen, S.; Lee, J.; Singh, N.; Krämer, S.; Stucky, G. D.; Moskovits, M. An Au-
445 tonomous Photosynthetic Device in Which All Charge Carriers Derive from Surface
446 Plasmons. *Nature Nanotechnology* **2013**, *8*, 247–251.

447 (9) Marimuthu, A.; Zhang, J.; Linic, S. Tuning Selectivity in Propylene Epoxidation by
448 Plasmon Mediated Photo-Switching of Cu Oxidation State. *Science* **2013**, *339*, 1590–
449 1593.

450 (10) Christopher, P.; Xin, H.; Linic, S. Visible-Light-Enhanced Catalytic Oxidation Reac-
451 tions on Plasmonic Silver Nanostructures. *Nature Chemistry* **2011**, *3*, 467–472.

452 (11) Wu, B.; Liu, D.; Mubeen, S.; Chuong, T. T.; Moskovits, M.; Stucky, G. D. Anisotropic
453 Growth of TiO2 onto Gold Nanorods for Plasmon-Enhanced Hydrogen Production from
454 Water Reduction. *Journal of the American Chemical Society* **2016**, *138*, 1114–1117.

(12) Zhou, L.; Zhang, C.; McClain, M. J.; Manjavacas, A.; Krauter, C. M.; Tian, S.; Berg, F.; Everitt, H. O.; Carter, E. A.; Nordlander, P.; Halas, N. J. Aluminum Nanocrystals as a Plasmonic Photocatalyst for Hydrogen Dissociation. *Nano Letters* **2016**, *16*, 1478–1484.

(13) Mukherjee, S.; Zhou, L.; Goodman, A. M.; Large, N.; Ayala-Orozco, C.; Zhang, Y.; Nordlander, P.; Halas, N. J. Hot-Electron-Induced Dissociation of H2 on Gold Nanoparticles Supported on SiO2. *Journal of the American Chemical Society* **2014**, *136*, 64–67.

(14) Mubeen, S.; Lee, J.; Liu, D.; Stucky, G. D.; Moskovits, M. Panchromatic Photoproduction of H2 with Surface Plasmons. *Nano Letters* **2015**, *15*, 2132–2136.

(15) Robatjazi, H.; Zhao, H.; Swearer, D. F.; Hogan, N. J.; Zhou, L.; Alabastri, A.; McClain, M. J.; Nordlander, P.; Halas, N. J. Plasmon-Induced Selective Carbon Dioxide Conversion on Earth-Abundant Aluminum-Cuprous Oxide Antenna-Reactor Nanoparticles. *Nature Communications* **2017**, *8*, 27.

(16) DuChene, J. S.; Tagliabue, G.; Welch, A. J.; Cheng, W.-H.; Atwater, H. A. Hot Hole Collection and Photoelectrochemical CO2 Reduction with Plasmonic Au/p-GaN Photocathodes. *Nano Letters* **2018**, *18*, 2545–2550.

(17) Clark, M. L.; Ge, A.; Videla, P. E.; Rudshteyn, B.; Miller, C. J.; Song, J.; Batista, V. S.; Lian, T.; Kubiak, C. P. CO2 Reduction Catalysts on Gold Electrode Surfaces Influenced by Large Electric Fields. *Journal of the American Chemical Society* **2018**, *140*, 17643–17655.

(18) Li, J.; Cushing, S. K.; Zheng, P.; Senty, T.; Meng, F.; Bristow, A. D.; Manivannan, A.; Wu, N. Solar Hydrogen Generation by a CdS-Au-TiO2 Sandwich Nanorod Array Enhanced with Au Nanoparticle as Electron Relay and Plasmonic Photosensitizer. *Journal of the American Chemical Society* **2014**, *136*, 8438–8449.

479 (19) Furube, A.; Du, L.; Hara, K.; Katoh, R.; Tachiya, M. Ultrafast Plasmon-Induced Elec-
480 tron Transfer from Gold Nanodots into TiO2 Nanoparticles. *Journal of the American*
481 *Chemical Society* **2007**, *129*, 14852–14853.

482 (20) Tian, Y.; Tatsuma, T. Mechanisms and Applications of Plasmon-Induced Charge Sepa-
483 ration at TiO2 Films Loaded with Gold Nanoparticles. *Journal of the American Chem-*
484 *ical Society* **2005**, *127*, 7632–7637.

485 (21) Mubeen, S.; Hernandez-Sosa, G.; Moses, D.; Lee, J.; Moskovits, M. Plasmonic Pho-
486 tosensitization of a Wide Band Gap Semiconductor: Converting Plasmons to Charge
487 Carriers. *Nano Letters* **2011**, *11*, 5548–5552.

488 (22) Tisdale, W. A.; Williams, K. J.; Timp, B. A.; Norris, D. J.; Aydil, E. S.; Zhu, X.-Y. Hot-
489 Electron Transfer from Semiconductor Nanocrystals. *Science* **2010**, *328*, 1543–1547.

490 (23) Tagliabue, G.; DuChene, J. S.; Abdellah, M.; Habib, A.; Hattori, Y.; Zheng, K.; Can-
491 ton, S. E.; Gosztola, D. J.; Cheng, W.-H.; Sá, J.; Atwater, H. A. Ultrafast Studies of
492 Hot-Hole Dynamics in Au/p-GaN Heterostructures. 12.

493 (24) Du, L.; Furube, A.; Hara, K.; Katoh, R.; Tachiya, M. Ultrafast Plasmon Induced
494 Electron Injection Mechanism in Gold–TiO2 Nanoparticle System. *Journal of Photo-*
495 *chemistry and Photobiology C: Photochemistry Reviews* **2013**, *15*, 21–30.

496 (25) Wen, X.; Xu, W.; Zhao, W.; Khurgin, J. B.; Xiong, Q. Plasmonic Hot Carriers-
497 Controlled Second Harmonic Generation in WSe2 Bilayers. *Nano Letters* **2018**, *18*,
498 1686–1692.

499 (26) Yu, Y.; Ji, Z.; Zu, S.; Du, B.; Kang, Y.; Li, Z.; Zhou, Z.; Shi, K.; Fang, Z. Ultrafast
500 Plasmonic Hot Electron Transfer in Au Nanoantenna/MoS2 Heterostructures. *Advanced*
501 *Functional Materials* **2016**, *26*, 6394–6401.

502 (27) Anderson, N. A.; Lian, T. ULTRAFAST ELECTRON TRANSFER AT THE
503 MOLECULE-SEMICONDUCTOR NANOPARTICLE INTERFACE. *Annual Review*
504 *of Physical Chemistry* **2005**, *56*, 491–519.

505 (28) Grimaldi, G.; Crisp, R. W.; ten Brinck, S.; Zapata, F.; van Ouwendorp, M.; Renaud, N.;
506 Kirkwood, N.; Evers, W. H.; Kinge, S.; Infante, I.; Siebbeles, L. D. A.; Houtepen, A. J.
507 Hot-Electron Transfer in Quantum-Dot Heterojunction Films. *Nature Communications*
508 **2018**, *9*, 2310.

509 (29) Sundararaman, R.; Narang, P.; Jermyn, A. S.; Goddard Iii, W. A.; Atwater, H. A. The-
510 oretical Predictions for Hot-Carrier Generation from Surface Plasmon Decay. *Nature*
511 *Communications* **2014**, *5*, 5788.

512 (30) Brown, A. M.; Sundararaman, R.; Narang, P.; Goddard, W. A.; Atwater, H. A. Nonra-
513 diative Plasmon Decay and Hot Carrier Dynamics: Effects of Phonons, Surfaces, and
514 Geometry. *ACS Nano* **2016**, *10*, 957–966.

515 (31) Govorov, A. O.; Zhang, H.; Gun'ko, Y. K. Theory of Photoinjection of Hot Plasmonic
516 Carriers from Metal Nanostructures into Semiconductors and Surface Molecules. *The*
517 *Journal of Physical Chemistry C* **2013**, *117*, 16616–16631.

518 (32) Zhou, J.-J.; Hellman, O.; Bernardi, M. Electron-Phonon Scattering in the Presence of
519 Soft Modes and Electron Mobility in $SrTiO_3$ Perovskite from First Principles. *Physical*
520 *Review Letters* **2018**, *121*, 226603.

521 (33) Bernardi, M.; Vigil-Fowler, D.; Lischner, J.; Neaton, J. B.; Louie, S. G. Ab Initio Study
522 of Hot Carriers in the First Picosecond after Sunlight Absorption in Silicon. *Physical*
523 *Review Letters* **2014**, *112*, 257402.

524 (34) Bernardi, M.; Mustafa, J.; Neaton, J. B.; Louie, S. G. Theory and Computation of Hot
525 Carriers Generated by Surface Plasmon Polaritons in Noble Metals. *Nature Communi-*
526 *cations* **2015**, *6*, 7044.

527 (35) Jhalani, V. A.; Zhou, J.-J.; Bernardi, M. Ultrafast Hot Carrier Dynamics in GaN and
528 Its Impact on the Efficiency Droop. *Nano Letters* **2017**, *17*, 5012–5019.

529 (36) Marcus, R. A. On the Theory of Oxidation-Reduction Reactions Involving Electron
530 Transfer. I. *The Journal of Chemical Physics* **1956**, *24*, 966–978.

531 (37) Wei, H.; Luo, J.-W.; Li, S.-S.; Wang, L.-W. Revealing the Origin of Fast Electron
532 Transfer in TiO2-Based Dye-Sensitized Solar Cells. *Journal of the American Chemical*
533 *Society* **2016**, *138*, 8165–8174.

534 (38) Liu, Y.-Y.; Zheng, F.; Jiang, X.; Luo, J.-W.; Li, S.-S.; Wang, L.-W. *Ab Initio* Inves-
535 tigation of Charge Trapping Across the Crystalline- Si –Amorphous- Si O 2 Interface.
536 *Physical Review Applied* **2019**, *11*, 044058.

537 (39) Tarafder, K.; Surendranath, Y.; Olshansky, J. H.; Alivisatos, A. P.; Wang, L.-W. Hole
538 Transfer Dynamics from a CdSe/CdS Quantum Rod to a Tethered Ferrocene Derivative.
539 *Journal of the American Chemical Society* **2014**, *136*, 5121–5131.

540 (40) Chu, I.-H.; Radulaski, M.; Vukmirovic, N.; Cheng, H.-P.; Wang, L.-W. Charge Trans-
541 port in a Quantum Dot Supercrystal. *The Journal of Physical Chemistry C* **2011**, *115*,
542 21409–21415.

543 (41) Duncan, W. R.; Craig, C. F.; Prezhdo, O. V. Time-Domain Ab Initio Study of Charge
544 Relaxation and Recombination in Dye-Sensitized TiO2. *Journal of the American Chem-*
545 *ical Society* **2007**, *129*, 8528–8543.

546 (42) Prezhdo, O. V.; Duncan, W. R.; Prezhdo, V. V. Photoinduced Electron Dynamics
547 at the Chromophore–Semiconductor Interface: A Time-Domain Ab Initio Perspective.
548 *Progress in Surface Science* **2009**, *84*, 30–68.

549 (43) Zhang, J.; Guan, M.; Lischner, J.; Meng, S.; Prezhdo, O. V. Coexistence of Differ-

550 ent Charge-Transfer Mechanisms in the Hot-Carrier Dynamics of Hybrid Plasmonic
551 Nanomaterials. *Nano Letters* **2019**,

552 (44) Long, R.; Prezhdo, O. V. Instantaneous Generation of Charge-Separated State on TiO2
553 Surface Sensitized with Plasmonic Nanoparticles. *Journal of the American Chemical*
554 *Society* **2014**, *136*, 4343–4354.

555 (45) Zhang, Z.; Liu, L.; Fang, W.-H.; Long, R.; Tokina, M. V.; Prezhdo, O. V. Plasmon-
556 Mediated Electron Injection from Au Nanorods into MoS2: Traditional versus Pho-
557 toexcitation Mechanism. *Chem* **2018**, *4*, 1112–1127.

558 (46) Long, R.; Prezhdo, O. V. Ab Initio Nonadiabatic Molecular Dynamics of the Ultrafast
559 Electron Injection from a PbSe Quantum Dot into the TiO2 Surface. *Journal of the*
560 *American Chemical Society* **2011**, *133*, 19240–19249.

561 (47) Zhang, J.; Hong, H.; Zhang, J.; Fu, H.; You, P.; Lischner, J.; Liu, K.; Kaxiras, E.;
562 Meng, S. New Pathway for Hot Electron Relaxation in Two-Dimensional Heterostruc-
563 tures. *Nano Letters* **2018**, *18*, 6057–6063.

564 (48) Long, R.; English, N. J.; Prezhdo, O. V. Photo-Induced Charge Separation across the
565 Graphene–TiO2 Interface Is Faster than Energy Losses: A Time-Domain Ab Initio
566 Analysis. *Journal of the American Chemical Society* **2012**, *134*, 14238–14248.

567 (49) Zhou, X.; Tokina, M. V.; Tomko, J. A.; Braun, J. L.; Hopkins, P. E.; Prezhdo, O. V.
568 Thin Ti Adhesion Layer Breaks Bottleneck to Hot Hole Relaxation in Au Films. *The*
569 *Journal of Chemical Physics* **2019**, *150*, 184701.

570 (50) Nam, Y.; Li, L.; Lee, J. Y.; Prezhdo, O. V. Strong Influence of Oxygen Vacancy Location
571 on Charge Carrier Losses in Reduced TiO_2 Nanoparticles. *The Journal of Physical*
572 *Chemistry Letters* **2019**, *10*, 2676–2683.

573 (51) Senanayake, R. D.; Guidez, E. B.; Neukirch, A. J.; Prezhdo, O. V.; Aikens, C. M. Theoretical Investigation of Relaxation Dynamics in Au $_{38}$ (SH) $_{24}$ Thiolate-Protected Gold Nanoclusters. *The Journal of Physical Chemistry C* **2018**, *122*, 16380–16388.

576 (52) Kang, J.; Wang, L.-W. Nonadiabatic Molecular Dynamics with Decoherence and Detailed Balance under a Density Matrix Ensemble Formalism. *Physical Review B* **2019**, *99*, 224303.

579 (53) Ren, J.; Vukmirović, N.; Wang, L.-W. Nonadiabatic Molecular Dynamics Simulation for Carrier Transport in a Pentathiophene Butyric Acid Monolayer. *Physical Review B* **2013**, *87*, 205117.

582 (54) Lymperakis, L.; Neugebauer, J.; Himmerlich, M.; Krischok, S.; Rink, M.; Kröger, J.; Polyakov, V. M. Adsorption and Desorption of Hydrogen at Nonpolar GaN(1-100) Surfaces: Kinetics and Impact on Surface Vibrational and Electronic Properties. *Physical Review B* **2017**, *95*.

586 (55) Fadley, C.; Shirley, D. Electronic Densities of States from X-Ray Photoelectron Spectroscopy. *Journal of Research of the National Bureau of Standards Section A: Physics and Chemistry* **1970**, *74A*, 543.

589 (56) Hinuma, Y.; Grüneis, A.; Kresse, G.; Oba, F. Band Alignment of Semiconductors from Density-Functional Theory and Many-Body Perturbation Theory. *Physical Review B* **2014**, *90*.

592 (57) Stevanović, V.; Lany, S.; S. Ginley, D.; Tumas, W.; Zunger, A. Assessing Capability of Semiconductors to Split Water Using Ionization Potentials and Electron Affinities Only. *Physical Chemistry Chemical Physics* **2014**, *16*, 3706–3714.

595 (58) Beach, J. D.; Collins, R. T.; Turner, J. A. Band-Edge Potentials of n-Type and p-Type GaN. *Journal of The Electrochemical Society* **2003**, *150*, A899.

597 (59) Singh-Miller, N. E.; Marzari, N. Surface Energies, Work Functions, and Surface Relax-
598 ations of Low-Index Metallic Surfaces from First Principles. *Physical Review B* **2009**,
599 *80*.

600 (60) Jacobi, K.; Zwicker, G.; Gutmann, A. Work Function, Electron Affinity and Band
601 Bending of Zinc Oxide Surfaces. *Surface Science* **1984**, *141*, 109–125.

602 (61) Matsumoto, Y.; Yoshikawa, T.; Sato, E.-i. Dependence of the Band Bending of the
603 Oxide Semiconductors on pH. *Journal of The Electrochemical Society* **1989**, *136*, 1389–
604 1391.

605 (62) Jia, W.; Cao, Z.; Wang, L.; Fu, J.; Chi, X.; Gao, W.; Wang, L.-W. The Analysis of
606 a Plane Wave Pseudopotential Density Functional Theory Code on a GPU Machine.
607 *Computer Physics Communications* **2013**, *184*, 9–18.

608 (63) Jia, W.; Fu, J.; Cao, Z.; Wang, L.; Chi, X.; Gao, W.; Wang, L.-W. Fast Plane Wave
609 Density Functional Theory Molecular Dynamics Calculations on Multi-GPU Machines.
610 *Journal of Computational Physics* **2013**, *251*, 102–115.

611 (64) Perdew, J. P.; Burke, K.; Ernzerhof, M. Generalized Gradient Approximation Made
612 Simple. *Physical Review Letters* **1996**, *77*, 3865–3868.

613 (65) Hamann, D. R. Optimized Norm-Conserving Vanderbilt Pseudopotentials. *Physical Re-*
614 *view B* **2013**, *88*, 085117.